OPTIMAL PROCESS PARAMETERS FOR *IN SITU* ALLOYED Ti15Mo STRUCTURES BY LASER POWDER BED FUSION

T.C. Dzogbewu*, I. Yadroitsev*, P. Krakhmalev**, I. Yadroitsava*, and A. Du Plessis***

* Department of Mechanical and Mechatronic Engineering, Bloemfontein, Central University of Technology, Free State, South Africa, 9300
** Department of Engineering and Physics, Karlstad University, Sweden, 651 88
*** University of Stellenbosch, Private Bag X1, Matieland, Stellenbosch, South Africa, 7602

Abstract

Powder Bed Fusion (PBF) is a manufacturing method with the advantage that it can produce objects of complex geometry. Additionally, it opens great opportunities to synthesize new materials from elemental powder using an *in situ* alloying approach. Potential of the *in situ* PBF alloying approach is nevertheless not well understood due to lack of experimental knowledge and information on the influence of process parameters on the microstructure, homogeneity and properties of the final materials. This investigation is focused on Ti15Mo alloy that was chosen as a promising β-type alloy for biomedical applications due to low Young's modulus, close to the mechanical properties of bones. Geometrical characteristics of single tracks were investigated at a wide range of laser powers and scanning speeds. Threshold of enthalpy ratio to transition from conduction to keyhole mode was found. To study the distributions of molybdenum in Ti matrix, X-ray nanoCT scans and SEM EDS were performed. Effects of hatch distance and scanning strategy on the layer surface morphology were investigated. Microstructure and mechanical properties of as-built specimens were analyzed. Illustrated effects of each process parameter on the synthesized material is paramount to successful manufacturing of advanced implants with mechanical properties close to bones.

Introduction

Titanium alloys are used extensively for biomedical applications due to its outstanding biological response. Ti6Al4V alloy is leading material for bone replacement since it is a light weight and biocompatible material, but the mismatch of the elastic modulus between Ti6Al4V implant and bone tissue is one of the major causes of stress shielding, bone resorption and implant loosening (Doh *et al.*, 2011; Lee *et al.*, 2013). The search for a more suitable alternative alloy for manufacturing direct load bearing structural implants has focused on β-type titanium alloys due to the fact that bone tissues respond better in β-type alloys than in (α+β)-type Ti alloys (Niinomi *et al.*, 1999; Nasab *et al.*, 2010; Disegi *et al.*, 2016).

The mechanical properties of Ti15Mo are suitable for structural biomedical applications (ASTM F2066-13). Novel β-type alloys with low modulus were also manufactured by Laser Powder Bed Fusion (LPBF). Vrancken *et al.* (2014) studied LPBF *in situ* alloying Ti6Al4V and 10%Mo powders. Mo particles were 5–10 μm is size, after sintering residual Mo particles (0.8 volume percent of material) did not seem to affect the mechanical properties. It was found that this LPBF alloy combines high strength (UTS of 919 MPa) with excellent ductility (elongation at

break was 20.1%) and has a low Young's modulus (73 GPa). It is therefore important to unearth the promising biomaterial properties of the alloy with relatively newer LPBF technology to harness the full potential of the alloy for biomedical applications.

Since the PBF process essentially consists of single tracks, which are placed side by side and superpositioned on each other to form a 3D object, it is indispensable to thoroughly understand the characteristics of the single tracks which form the final 3D objects. It is empirically proven that the formability, microstructure, mechanical properties and residual stress of LPBF parts are all determined by the nature of the single tracks, which are governed by the molten pool dynamics (Yadroitsev, 2009; Fischer *et al.*, 2003; Khairallah and Anderson, 2014; Körner *et al.*, 2011). Thus, manufacturing of high-quality LPBF parts is generally based on manufacturing of stable tracks with regular geometrical characteristics and good penetration into the previous layer to provide good adhesion. Properties of the manufactured parts depend strongly on each single laser-melted track and each single layer, as well as the strength of the connections between them (Yadroitsev, 2009).

During laser irradiation of a powder bed, if the laser energy intensity is moderate and the heat transport is mediated *via* conduction and convection within the molten pool without any obvious vaporization, the melting process is called conduction mode. However, if the processing parameters exceed a certain threshold, the mode of thermal conduction in the molten pool could change to the keyhole mode. In the keyhole mode, the laser energy density is sufficient to cause evaporation of the metal leading to plasma (vapor) formation. The vapor formation enhances laser energy absorption into the substrate and subsequent 'drilling' of the substrate. The collapse of the vapor cavity could leave a void (pore) which contributes to defects of the final product (Rai *et al.*, 2007; King *et al*., 2014; Verhaeghe *et al*., 2009; Khairallah *et al*., 2016; King *et al*., 2014). The two modes of conduction determine the type of formability, microstructure and mechanical properties of the final 3D parts. The literature reveals that conduction and keyhole modes have its peculiar advantages and disadvantages (Yang *et al*., 2016). A systematic experiment to determine the process parameters at which these two types of melting take place for Ti15Mo powder is therefore very important. A comprehensive knowledge of the process parameters at which a particular mode of conduction takes place would enable the operating engineer to produce tailored implants for a specific purpose.

In this research, Ti15Mo alloy was manufactured *in situ* by LPBF from elemental powders. Geometrical characteristics of single tracks were investigated at a wide range of laser powers and scanning speeds. Threshold of enthalpy ratio to transition from conduction to keyhole mode was found. To study the distributions of molybdenum, nanoCT scans and SEM EDS were performed. Effects of hatch distance and scanning strategy on the layer surface morphology were investigated. Microstructure and mechanical properties of as-built specimens were analyzed. Illustrated effects of each process parameter on the synthesized material is paramount to successful manufacturing of non-porous samples for advanced implants with mechanical properties close to bones.

Materials and methods

The experiments were conducted with pure Ti (CP Ti, grade 2) and Mo powders procured from TLS Technik GmbH & Co Spezialpulver KG. The Ti and Mo powders were spherical gas-atomized powders. The Ti powder has the following chemical composition in wt.%: Ti (bal.), O (0.17), Fe (0.062), C (0.006), H (0.002), N (0.012). The 10^{th}, 50^{th} and 90^{th} percentiles of equivalent diameter (weighted by volume) of the powder Ti particles were d_{10}=11.6 μm, d_{50}=24.6 μm and d_{90}=38.4 μm, for Mo powder they were d_{10}=*10.9* μm, d_{50}=22.4 μm and d_{90}=31.9 μm. 85 wt.% of the CP Ti powder was mechanically mixed with 15 wt.% of the Mo. The mixture was dried in an oven for about 15 h at the temperature of 85°C. The powder mixture was stirred at 30 min to ensure the heating is evenly done to enhance free flowing of the powder.

The experiments were conducted on EOSINT M280 machine (EOS GmbH). The laser spot diameter was 80 μm. For single tracks and layers experiments, a uniform powder layer of 60 μm thickness was deposited on the CP Ti substrate. Single tracks were sintered over a wide range of laser powers (P=50–350 W) and scanning speeds (V=0.08–3.4 m/s). All tracks were of length 20 mm. For each scanning speed, three single scan lines were produced.

To investigate the distribution of elements in the bulk, 3D rectangular specimens of 10x10 mm and 5 mm in height were manufactured at 150 and 350 W laser powers, 1.0 and 2.4 m/s scanning speeds, 80 μm hatch distance and 30 μm layer thickness. For analysis of the cross-sections, samples were cut, grinded, polished, and subsequently etched with Kroll's reagent. The microstructural examinations of the single tracks, single layers and 3D objects were conducted by an optical microscope (OM). For the single tracks, measurements were made of the width of the tracks, the height of the tracks above the substrate and the depth of the tracks into the substrate. Vickers hardness of the samples was measured at 200 gf loading by test in polished cross-sections cut perpendicular to the building direction (40 measurements for each cross-section).

X-ray CT scans were performed at the Stellenbosch CT facility (du Plessis *et al.* 2016) making use of a nanoCT instrument (General Electric NanotomS), using 120 kV and 130 μA for X-ray generation and setting the voxel size to 2.5 μm. Image analysis of CT scans was performed in Volume Graphics VGStudioMax 3.0. A global threshold was chosen based on grey value histogram of the entire volumetric data set, then a local optimization was performed at every point for steepest grey-value gradient at interface between two materials. This method is called "advanced surface determination" (du Plessis *et al.*, 2016) and the analysis was performed on the region selected from this determination, using the defect analysis function, applied to Mo particles as inclusions.

The distribution of Mo in CP Ti was done with Scanning Electron Microscope (SEM). Surface roughness of the single layers was measured with Surftest SJ-210 portable surface roughness tester accordingly to ISO 1997. The samples for tensile test were prepared according to E8/E8M ASTM standard. The tensile tests were carry out using MTS Criterion Model 43 Electromechanical Universal Test System machine at room temperature with strain rate of 0.5 mm/min.

Results

The quality, reproducibility, and reliability of LPBF parts are dependent on the quality of the sintered single tracks and layers. Single tracks produced by LPBF could be discontinuous due to the balling effect or have irregular geometrical characteristics from satellites, or from excessive energy input, when keyhole mode occurs. Therefore, it was necessary to find a process parameter window that guarantees manufacturing of high-quality regular tracks. The process map in Figure 1 reveals the combination of process parameters that yield continuous tracks, those which cause the pre-balling effect, when the liquid cylinder was irregularly broken and the balling effect (spheroidisation of the melt pool and formation of beads). General top view of the tracks at similar linear energy input (ratio of the laser power *P* to the scanning speed *V*) is shown in Figure 2.

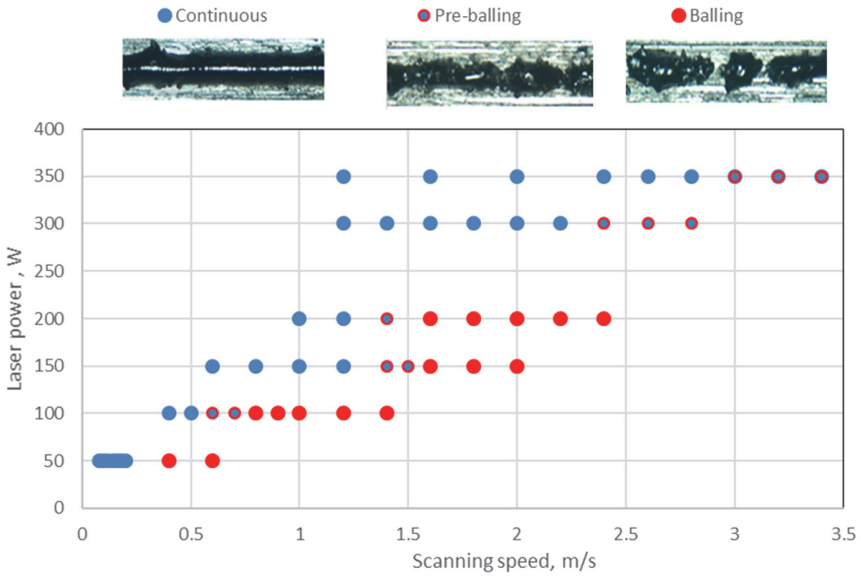

Figure 1: Process map for Ti15Mo single tracks produced at laser powers from 50 W to 350 W with varied scanning speeds (0.08–3.4 m/s).

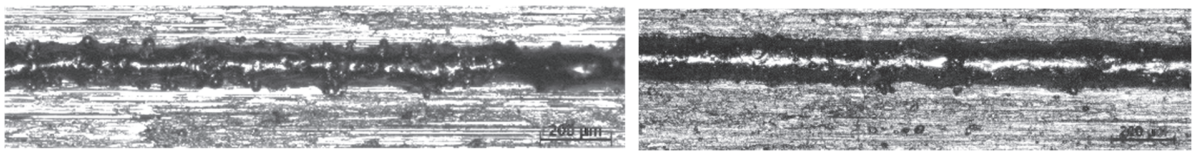

(a) (b)

Figure 2: Top view of the tracks at similar linear energy input (*P*/*V*~200 J/m): *P*=100 W, *V*=0.5 m/s (a) and *P*=350 W and *V*=1.6 m/s (b).

The measured dependence of track width on the scanning speed in the *in situ* alloyed Ti15Mo is presented in Figure 3. Analysis of the cross-sections showed that at chosen powder layer thickness of 60 µm and laser power of 50 W, the re-melted depth was low (about 10 µm).

Single tracks had only small metallurgical bonding with the substrate (Figure 4 and Figure 5a). At laser powers of 100, 150, 200, 300 and 350 W with scanning speeds ranging from 0.4-0.5, 0.6-1.2, 1.0-1.2, 1.8-2.2, and 2.4-2.8 m/s respectively the laser energy was enough to melt the powder completely and also the underlying material (substrate) to form a metallurgical bonding. A penetration depth is governed by laser power mainly, but also have a tendency to decrease with scanning speed (Figure 4). At laser powers of 300 W and 350 W and scanning speeds in the range of 1.2-1.6 m/s and 1.2-2.0 m/s respectively the penetration depth exceeded the height and width of the tracks 1.5-2 times (Figure 5c). It should be noted that in the current experiment there were no pores found at the keyhole mode in cross-sections of the tracks.

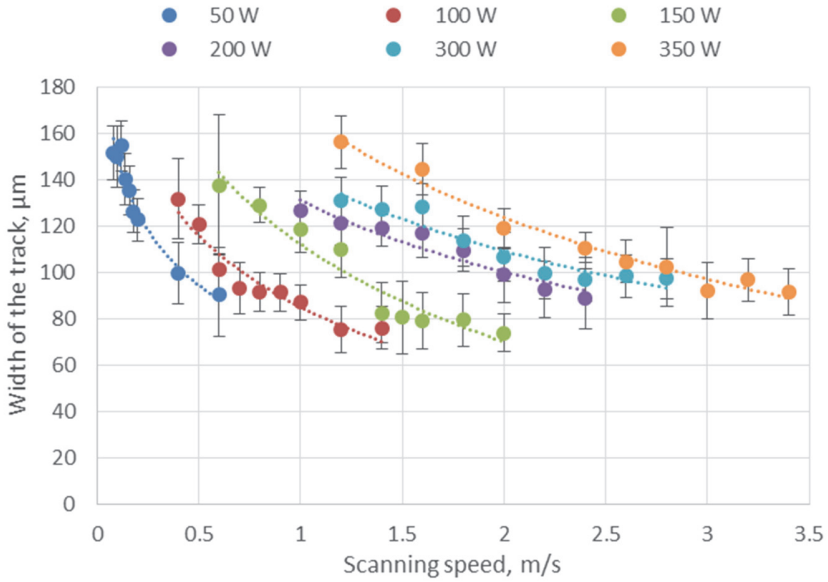

Figure 3: The width of the single tracks at different scanning speeds and laser powers.

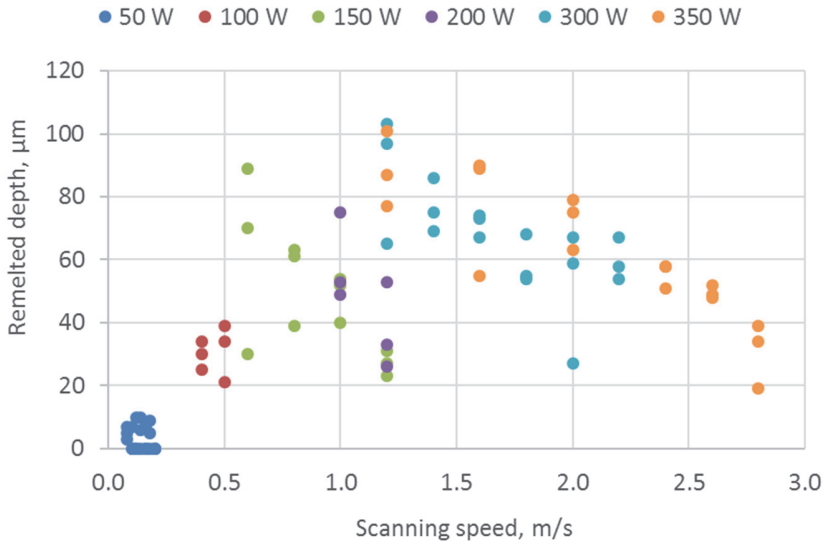

Figure 4: Remelted depth for continuous tracks at different scanning speeds and laser powers.

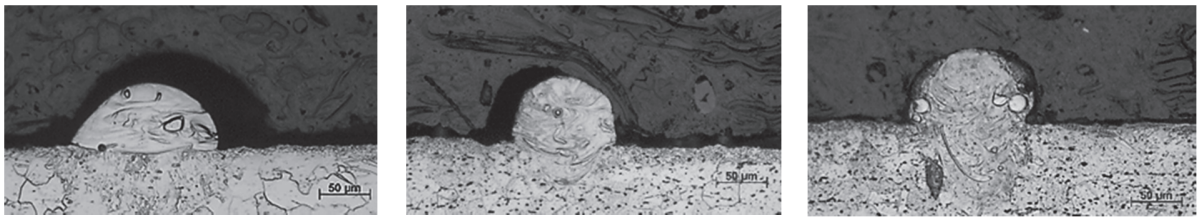

(a) (b) (c)

Figure 5: Cross-sectional view of single tracks demonstrating low penetration at P=50 W, V=0.1 m/s (a), conduction mode at P=150 W, V=1.0 m/s (b) and keyhole mode at P=300 W, V=1.4 m/s (c).

Express analysis of cross sections of single tracks showed presence of round particles (Figure 5) that were identified as incompletely molten Mo particles by SEM EDS. NanoCT scans were done to analyse how these Mo particles were distributed in the Ti matrix. Mo particles were completely or partially melted and randomly distributed in single tracks (Figure 6 and Figure 7).

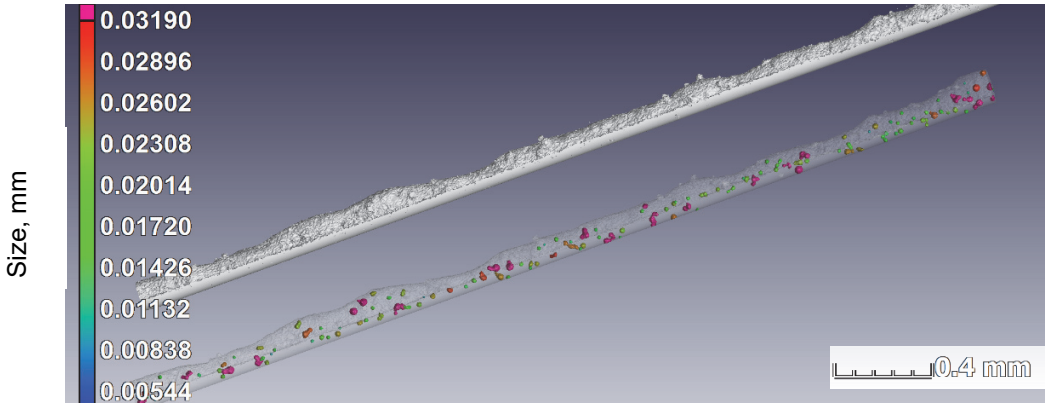

(a)

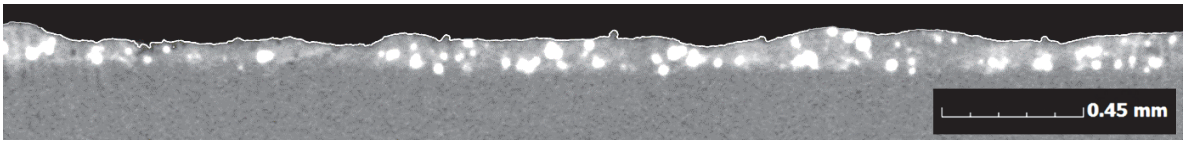

(b)

Figure 6: 3D reconstruction of the distribution Mo particles in single tracks (a) and cross-section (b) at 150 W laser power and 1.0 m/s scanning speed.

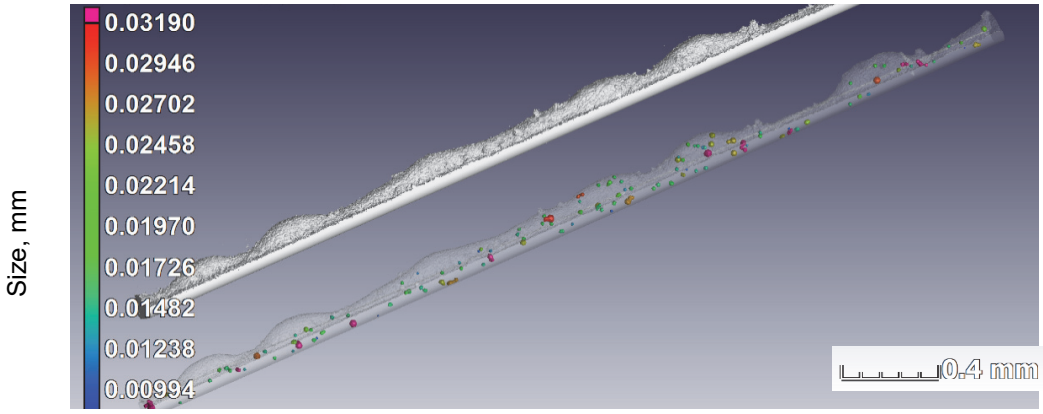

(a)

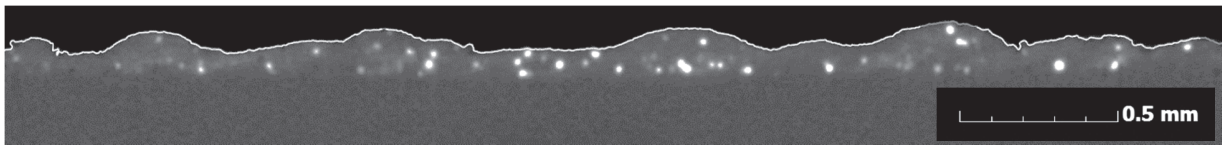

(b)

Figure 7: 3D reconstruction of the distribution Mo particles in single tracks (a) and cross-section (b) at 350 W laser power and 2.4 m/s scanning speed.

To investigate influence of scanning strategy on single layer morphology at different hatch distances of 80 µm, 90 µm and 100 µm, two different types of surfaces were produced: single scan and rescanning surfaces. Rescanning strategy would ensure that the laser could melt satellites and enhance homogeneity of *in situ* alloyed material (Figure 8).

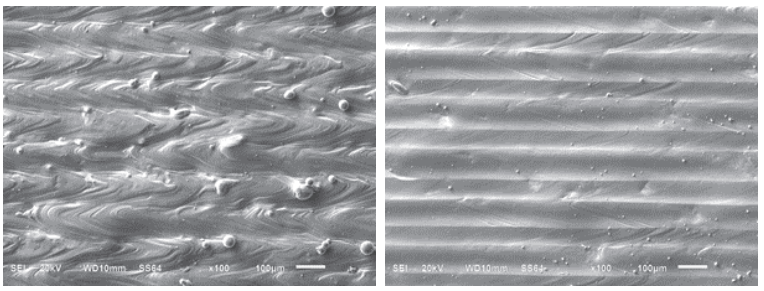

(a) (b)

(c) (d)

Figure 8: Top view of the surfaces at hatch distance of 80 µm and P= 150 W, V= 1.0 m/s (a, b) and P=350 W, V= 2.4 m/s (c, d) with single scan (a, c) and rescanning (b, d).

Rescanning considerably reduces surface roughness; the observed *Rz* value after rescanning was lower (Figure 9).

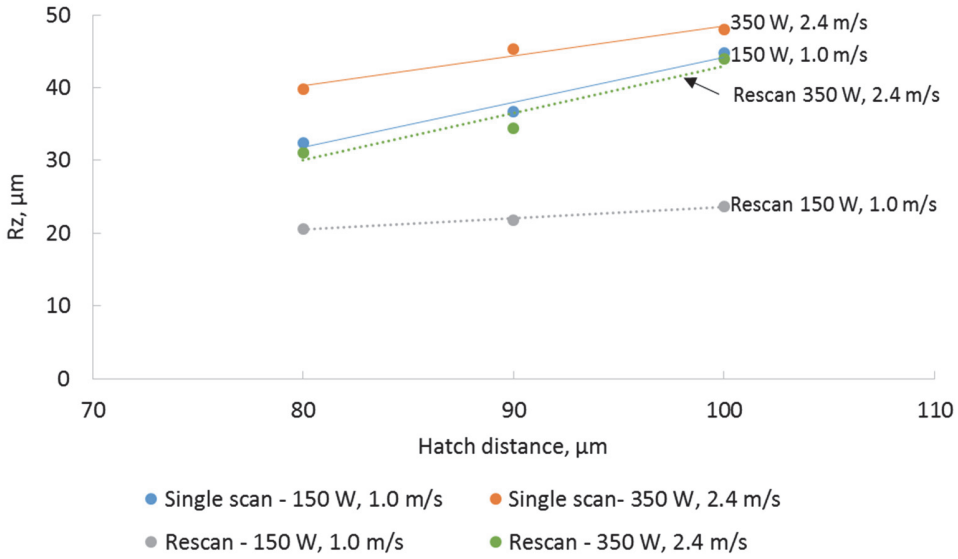

Figure 9: Surface roughness of *in situ* alloyed Ti15Mo at varied hatch distance, laser power and scanning speed.

An SEM EDS elemental map analysis was performed to investigate the distribution of the Mo at the surface of single layers of Ti15Mo alloy manufactured by LPBF (Figure 10). The cross-sectional examination of single layer of Ti15Mo LPBF alloy revealed that the Mo powder particles were not completely melted especially for the single scan samples (Figure 11 and Figure 12). Molybdenum was randomly distributed in the Ti alloy matrix in the layer, similar to the single tracks. In 3D LPBF samples, rescanning did not reduce the number of partially melted Mo particles even at 350 W laser power (Figure 13).

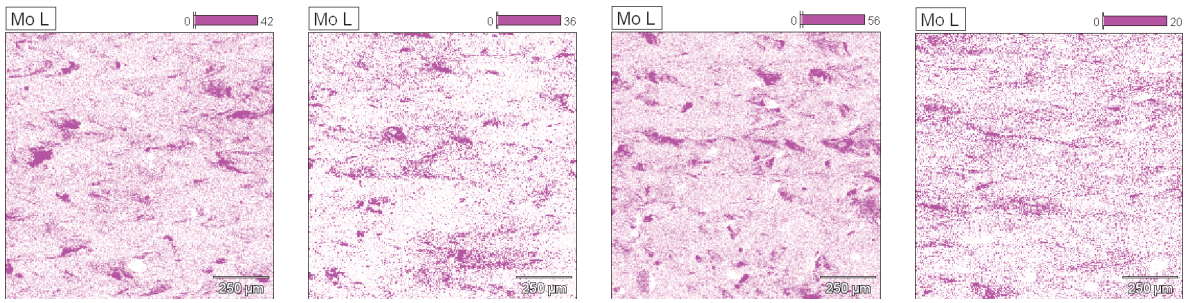

(a) (b) (c) (d)

Figure 10: Mo distribution map by SEM EDS spectra from Ti15Mo *in situ* alloy: (a) single scanning and (b) rescanning at laser power 150 W, scanning speed 1.0 m/s; (c) single scanning and (d) rescanning at laser power 350 W, scanning speed 2.4 m/s.

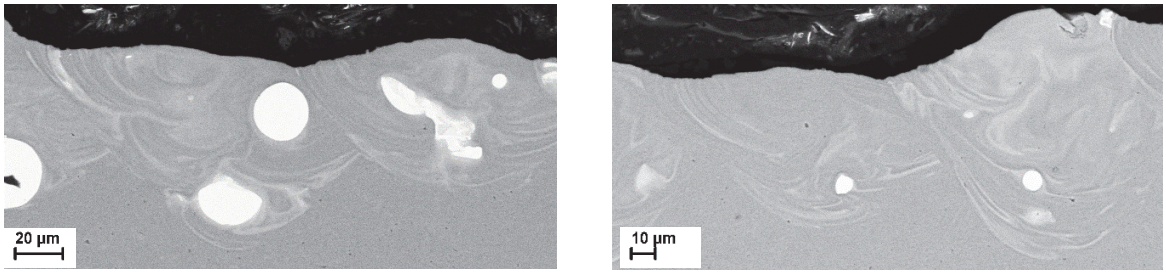

(a) (b)

Figure 11: Cross-sectional view of first layer after single scanning at 100 µm hatch distance: *P*=150 W, *V*=1.0 m/s (a) and *P*=350 W, *V*=2.4 m/s (b).

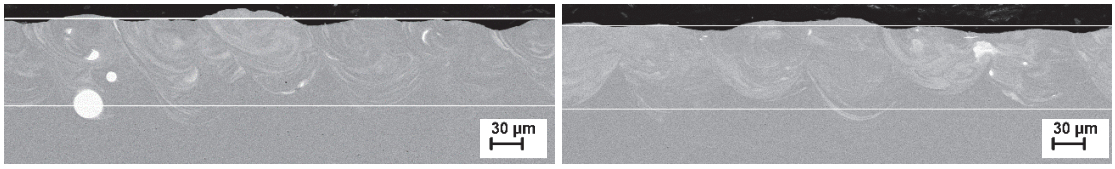

(a) (b)

Figure 12: Cross-sectional view of first layer after single scanning (a) and rescanning (b) at *P*=150 W, *V*= 1.0 m/s and 90 µm of hatch distance.

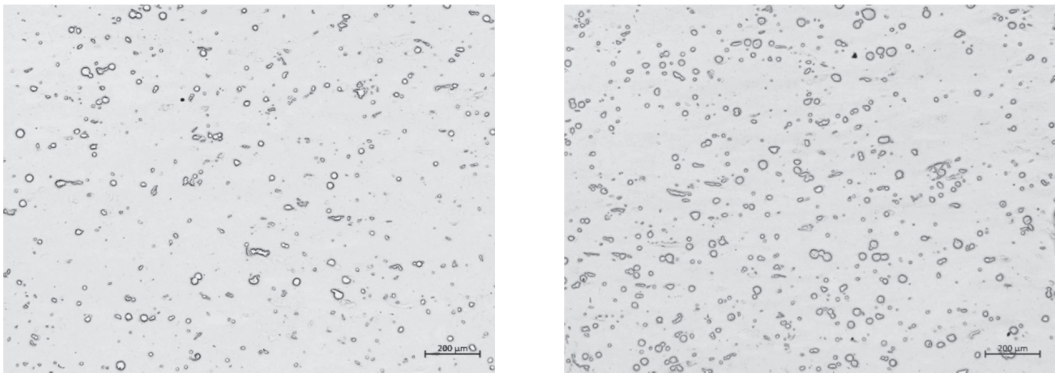

(a) (b)

Figure 13: Polished cross-sections of the LPBF cubes at 350 W laser power, 2.4 m/s scanning speed and 80 µm hatch distance: single scanning (a) and rescanning (b).

Analysis of the microstructure was done by means of optical and scanning electron microscopy. Optical microscopy of specimens etched with Kroll's reagent showed that the microstructure consists of a portion of lamellar structure, areas with cellular dendritic structure and unmolten particles of Mo. Boundaries of vertical colonies are also visible (Figure 14a). At the transverse plane the grains had more irregular shape at single scan strategy, well-defined grain boundaries were found in the rescanned samples (Figure 14b). The structure consists of regions of alpha hexagonal phase commonly forming lamellar structure and regions of β-cubic phase formed cellular dendritic structure during solidification (Figure 15). SEM observations of the manufactured samples demonstrated that the alloy was not homogeneous and areas enriched by Mo were observed. On average, the concentration of Mo in the alloy varied in the range of 7.5-15 wt%.

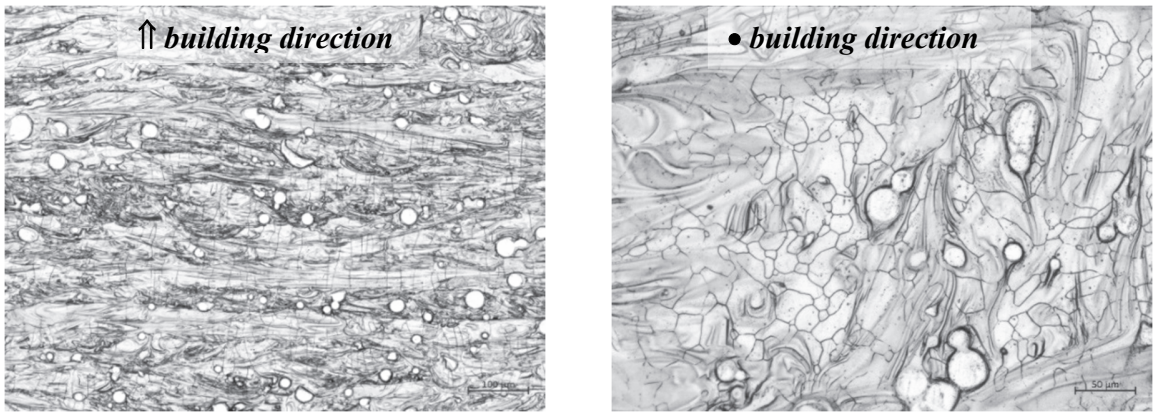

(a) (b)

Figure 14: Microstructure of cross-sections of the 3D LPBF samples at 150 W laser power, 1.0 m/s scanning speed and 80 µm hatch distance: single scanning (a) and rescanning (b).

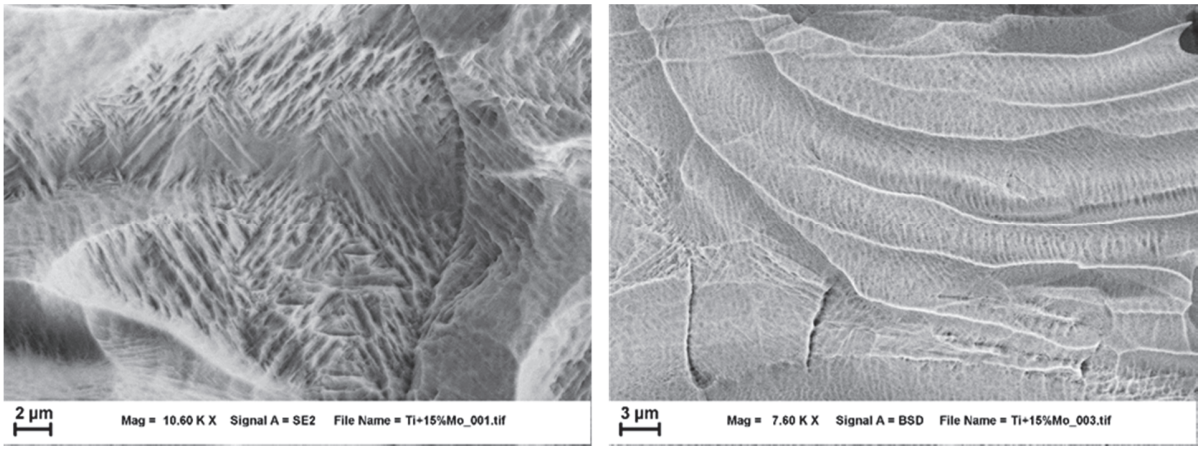

(a) (b)

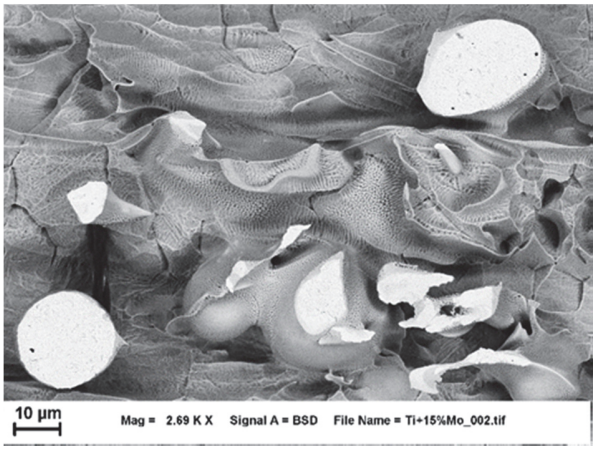

(c)

Figure 15: SEM photos of the lamellar (a) and dendritic structure (b); cellular dendritic structures associated with Mo particles (c) in LPBF Ti15Mo alloy.

Vickers hardness in LPBF samples produced at 150 and 350 W laser power did not differ (435±35 HV and 436±25 HV correspondingly); rescanning had no impact at hardness values (Figure 16).

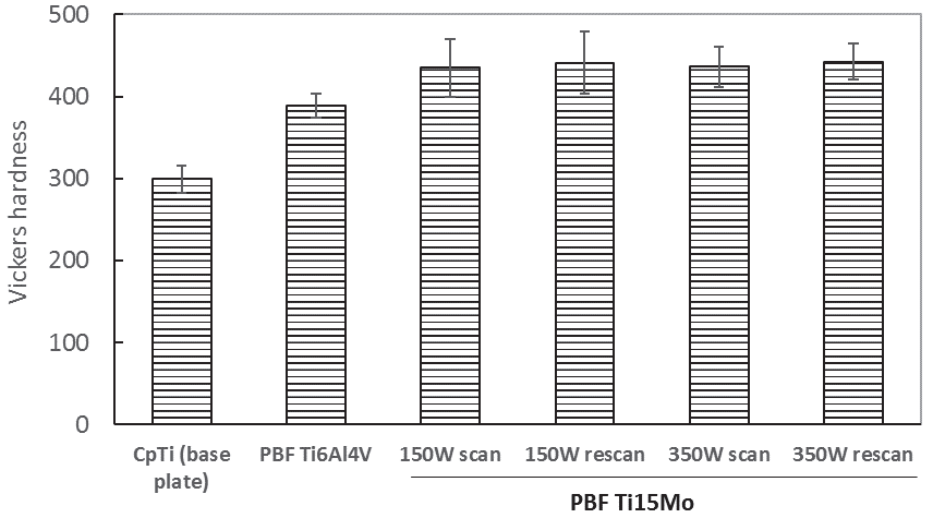

Figure 16: Vickers hardness of the base Ti plate and LPBF Ti15Mo alloy.

Discussion

It could be observed in Figure 1 that the range of scanning speeds for producing continuous single tracks increased with laser power. At higher laser power, temperature of the melt pool increased, which improved wetting and expanded zone for continuous tracks (Fischer *et al.*, 2003; Yadroitsev *et al*., 2007; Wang *et al.*, 2017). The track width was defined by laser power input *P* and the irradiation time (or scanning speed *V*) and it was limited by laser beam spot size (Figure 3). Leitz *et al*. (2015) studied LPBF of materials with high and low thermal conductivity such as molybdenum and steel manufactured in a similar fashion. It was shown that due to the high heat conductivity of Mo, the energy from the laser beam – matter interaction zone is transported away quite efficiently and in this case the melt pool size was mainly controlled by the laser power. For steel, that has lower thermal conductivity, the width of the molten pool was mainly determined by the irradiation, or interaction laser beam–matter time, i.e. laser scanning speed. In this investigation, single tracks from Ti15Mo powder were formed at the pure Ti substrate, *i.e.* low conductive material. At 50 W and scanning speed of 0.08 m/s, the width of the tracks was 152±11.7 μm. At laser power of 350 W and *V*=1.2 m/s, width of the track was almost the same (156±11.4 μm). Difference in the duration of laser beam–matter interaction changed from 1 ms to 0.07 ms. Thus, for *in situ* alloyed Ti15Mo material the dependence between process parameters and width of the track was more complicated, and not only conductivity but also other factors determined the track width.

The single track is formed from powder and substrate material under the laser beam. The powder particles from adjusted areas also involved into the melting process. Spattering and denudation effect led to creation of satellites, *i.e.* droplets at the edge of the tracks (Yadroitsev, 2009; Matilainen *et al.*, 2015). Satellites are surface defects and are formed due to melt

spattering and partial powder melting in peripheral zone of the laser spot. Aboulkhair *et al.* (2016) observed that at a constant laser power the number of satellites increases with increasing scanning speed. The experimental work of Mumtaz and Hopkinson (2010) demonstrated that the smaller the powder particle size the smaller the size of the satellites. It was generally reported that the number of satellites is much higher at lower laser power at similar linear energy input (*P/V)*. The same trend observed in the present investigation (Figure 2).

The remelted depth of single tracks depends on the properties of the material, the thickness of the powder layer and the power density of the laser radiation that is ratio of laser power to the area of spot size (Yadroitsev *et al.*, 2012). At higher laser power, the range of scanning speeds for manufacturing of high-quality continuous tracks increased and the dependence of the penetration depth on scanning speed was more pronounced (Figure 4).

The cross-section of solidified molten pool formed in conduction mode is about semi-circular in welding (Eagar & Tsai, 1983). At high energy input, a keyhole shape of the molten pool is a result of very pronounced fluid flow induced by thermocapillary forces and recoil pressure directs outward and upward (Wei*,* 2012). In LPBF, Yang *et al.* (2016) also described the morphology of single sintered tracks as semi-circular in the conduction mode and narrow and deep in the keyhole mode. In present study, the shape of the single tracks formed at laser powers of 100, 150, 200, 300 and 350 W and their corresponding scanning speeds of 0.4-0.5, 0.6-1.2, 1.0-1.2, 1.8-2.2, and 2.4-2.8 m/s respectively nearly resembled semi-circular shape. Such a mode leads to good bonding between the tracks and the substrate, hence could be referred to as optimum set of processing parameters (Figure 5b).

Hann *et al.* (2011) investigated laser welding and the effect of processing parameters on different materials in order to optimize the processing window. Base on the assumption that the ratio of the deposited energy density ΔH to the enthalpy at melting, or heat of fusion (h_s), the transition from conduction to keyhole mode can be predicted. Deposited laser energy density was expressed as

$$\Delta H = \frac{A \cdot C \cdot P}{\rho \cdot \sqrt{r_0^3 \cdot a \cdot V}} \qquad \text{Eq.1,}$$

where P is the laser power, V is the scanning speed, r_0 is the half-width of Gaussian beam spot at the surface, C is the constant, a is the thermal diffusivity, ρ is the density of the material and A is the absorptivity. King *et al.* (2014) followed a similar ratio to predict the conditions required for transition from conduction controlled melting to keyhole mode melting in LPBF. It was proposed that keyhole mode could be realized when penetration depth is greater than half the width of the tracks. This approach was efficiently used in this investigation. Measurements of a ratio of the remelted depth to the half width of Ti15Mo single tracks showed that keyhole mode occurred at P=150–350 W at low scanning speed (Figure 3 and Figure 4). The mixture of powders consists of 85% pure Ti, thus titanium properties were chosen for the calculation threshold enthalpy ratio. Laser spot size of 80 μm, 50–350 W laser power, scanning speeds for continuous tracks, enthalpy of melting of Ti is 435.4 J/g, C=1 and Eq. 1, were used for calculations. Figure 17 shows the ratio of remelted depth/half width *versus* the enthalpy ratio of the LPBF Ti15Mo

mixture. High laser energy input $\Delta H/h_s$ >70 led to narrow molten pool and deep penetration. Therefore, these processs parameters are not recommended for manufacturing LPBF tracks.

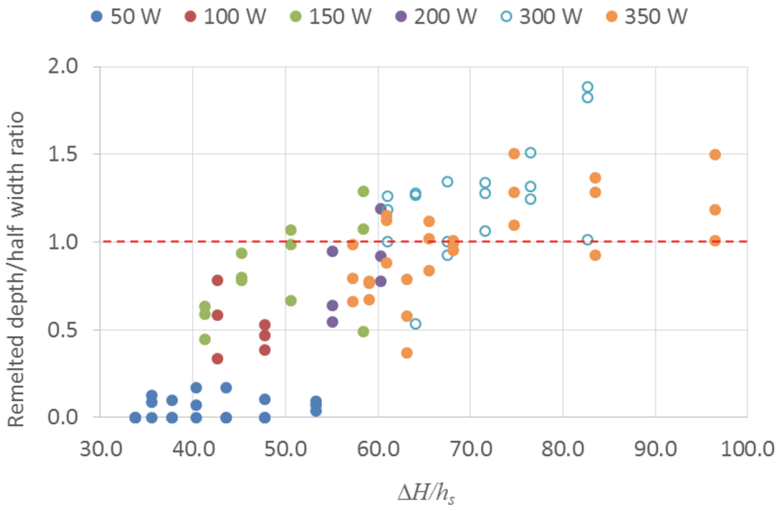

Figure 17: Ratio of remelted depth to half width of the single tracks *versus* enthalpy ratio.

The basic building units of LPBF objects are sets of single tracks. The previously solidified layer serves as the substrate for the subsequent layer-by-layer formation. The layer-wise process continues until the object is manufactured. The quality of the individual set of single tracks determines the morphology and mechanical properties of the final object (Yadroitsev *et al.,* 2015).

The modeling results of Qiu *et al.* (2015) predicted that the complex melt flow behavior within the melt pool could move in a dispersed and random way that could lead to different track head geometry. Due to the hydrodynamic movement, the geometry of the molten pool could deviate significantly resulting in different track head (height) shape. The complex melting process is governed by viscosity (Rayleigh instability), surface tension (Marangoni effect), capillarity effects, gravity, *etc.* (Yadroitsev *et al.*, 2010), which would lead to stochastic melt tracks with irregular and corrugated track head appearance (Chan *et al.*, 1987; Kou *et al.*, 2011; Körner *et al.*, 2011, 2013). Additionally, since the delivered powder layer consists of randomly packed powder particles, the molten pool formation comprises of different particles of varying sizes and consequently the layer thickness can vary. Figure 18 clearly demonstrates the uneven nature of the LPBF in situ manufactured Ti15Mo track heights.

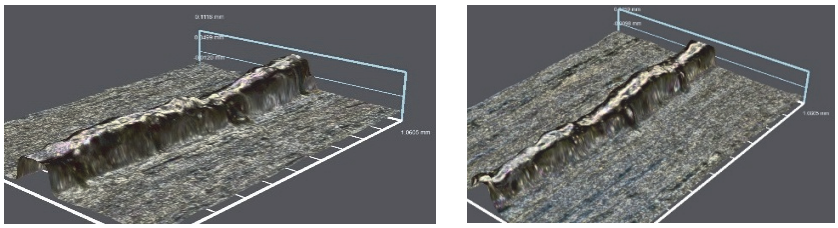

(a) (b)

Figure 18: Single tracks on the substrate at 150 W (a) and 350 W (b) laser power.

The layer-by-layer sintering of the irregular tracks would produce a rough surface. At higher scanning speeds, balling and humping effects are more pronounced in LPBF of single tracks (Yadroitsava *et al.*, 2015*).* The non-regular shape of single tracks causes inhomogeneous powder deposition in the next layer which would trigger inconsistency in melt flow in the subsequent layers. At the present time, there are no clear rules for the morphology of the synthesized LPBF layer, but it is definitely understood that the energy input should be sufficient to melt the delivered powder layer with irregular thickness formed due to the previous cycle of synthesis.

From the above analysis of the single tracks, optimum process parameters of 150 W and 350 W with corresponding scanning speeds of 1.0 m/s and 2.4 m/s respectively were selected to produce single layers from the same powder. To investigate influence of scanning strategy on single layer morphology at different hatch distances of 80 μm, 90 μm and 100 μm, two different types of surfaces were produced: single scan and rescanning surfaces. Rescanning strategy would ensure that the laser could melt satellites and enhance homogeneity of *in situ* alloyed material (Figure 8). It could be stated that surface roughness increases with increasing laser power and scanning speed and decreasing hatch distance (Figure 9). At a lower hatch distance, a larger surface area of the previously solidified layer was remelted which could melt any previously unmelted powder particles. Similar effects of an increase of the surface quality was shown for different materials manufactured by LPBF (Yasa & Kruth, 2008; Yadroitsev, 2009; Król *et al.*, 2014; Kruth *et al.*, 2009, 2010; Kinnear *et al.*, 2016).

Experimental results showed that surface roughness of single layer at 350 W laser power was higher than at 150 W. Estimated time of direct interaction of the laser beam with the surface of solid material under laser spot size is $t_{D.I.}=d_0/V$, where d_0 is laser beam spot size. For 80 μm laser spot size and scanning speeds V=2.4 and 1.0 m/s, time of laser-powder direct interaction was 33 μs and 80 μs respectively. Numerical simulations executed as described by Yadroitsev *et al.* (2015) showed that at 150 W laser power and scanning speed of 1.0 m/s, Ti molten pool existed about 30% longer than at 350 W and 2.4 m/s (Figure 19). The molten pool shape was more symmetrical and process was more stationary at 150 W: maximal depth of the molten pool from numerical simulations was found to be 52 μm and the length was 210 μm. At 350 W and 2.4 m/s scanning speed, the penetration depth was 52 μm, but the length increased up to 380 μm. The higher volume of the Ti molten pool and the temperature gradient increased with laser power, presumably causes instability of the molten pool. Since single layer consists of less regular tracks, surface roughness of the layer was higher at higher laser power and scanning speeds (Figure 9).

Optimization of the process parameters to enhance homogenous single layer formation is one of the first main steps to produce non-porous dense LPBF objects. Rescanning improved the distribution of the Mo in the single layer top surface. The rescanning process has effect on the homogeneity of Mo distribution at the surface, as a result of remelting of the layer. Partially molten molybdenum particles, which diminished in size due to the first melting, also were remelted for rescanning. The effect of the varied hatch distance nevertheless, does not have any significant effect on the Mo distribution at the top surface (Figure 10).

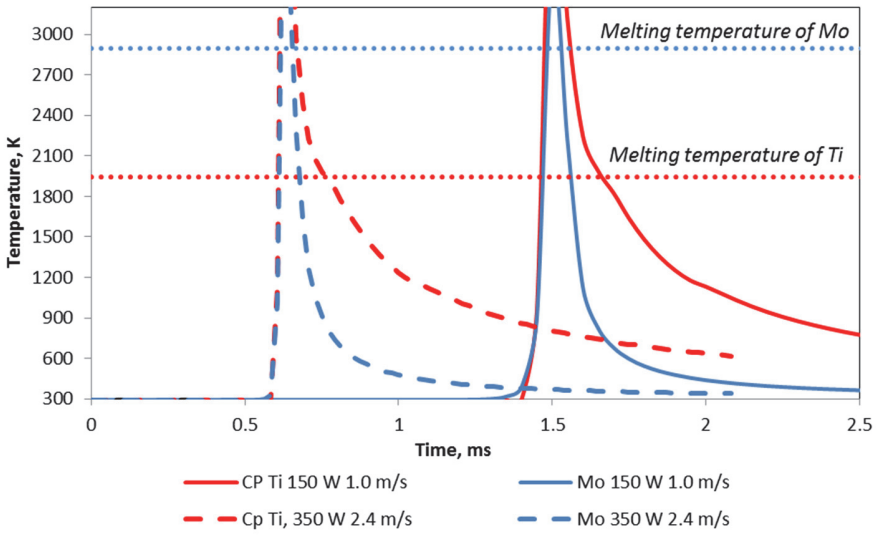

(a)

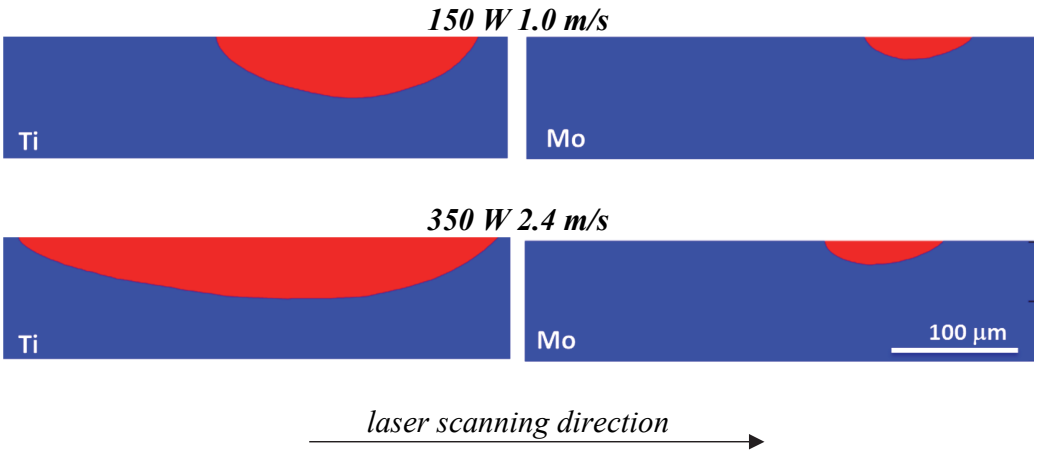

(b)

Figure 19: Temperature profile of the point on the surface of Ti or Mo bulk materials (a) and longitudinal cross-section of molten pools (b).

The cross-sectional examination of single tracks and layers of *in situ* LPBF alloyed Ti15Mo showed inhomogeneity of the fabricate objects (Figure 5, Figure 10–Figure 13). The observed effect of energy input on *in situ* alloying Ti and Mo powder mixture could be explained taking into account the vast difference in material properties. Ti and Mo have a specific heat capacity of 528 J/(kg×K) and 217 J/(kg×K), thermal conductivity of 17 W/(m×K) and 138 W/m×K, density of 4500 kg/m^3 and 10220 kg/m^3, latent heat of fusion of 435 kJ/kg and 293 kJ/kg, correspondingly. Taking into account latent heat of melting, heat capacity and density, energy for melting of unit volume of employed material was estimated: for bulk Ti and Mo these values are 5.82 J/mm^3 and 8.74 J/mm^3 respectively. Thus, the energy input needs to be higher by about 1.5 times to melt similar volumes of Mo compared to Ti.

At chosen process parameters, the input energy was sufficiently high to melt Ti particles completely but not all Mo powder due to the thermo-physical property differences between the two materials. The melting point for CP Ti is 1941 K and Mo is about 2896 K. Also, the laser radiation reflectance of Mo is higher than that of CP Ti (Palik, 1985), hence CP Ti powder would absorb more laser radiation than Mo. These factors led to the complete melting of CP Ti and partial melting of molybdenum at the selected manufacturing conditions and powder size distribution. The temperature homogenization time in solid particles could be calculated as $t_{hom}=r^2/a$, where r is the particle radius and a is the thermal diffusivity of bulk metal (Fisher *et al.*, 2003). The entire 25 μm diameter Mo powder particle became uniformly heated after about 2.5 μs, while Ti particle with similar diameter needed 22 μs. The estimated time of the existing molten pool for Mo was determined mainly by laser power: it was about 45 μs and 30 μs for 350 W and 150 W correspondingly. Since high laser power caused high temperature during LPBF, Mo particles were melted to a greater degree at laser power 350 W in comparison with 150 W (Figure 6b and Figure 7b). Size of d_{90} weighted by volume for non-melted and partially melted Mo particles and their agglomerates in the single tracks were 25.6 μm for 350 W laser power and 44.8 μm for 150 W. Initially, Mo powder particles had d_{90}=31.9 μm. This result indicates that preferentially the largest particles were least melted in single tracks.

From numerical simulations of laser scanning of bulk material was found that penetration depth for pure Mo was 11 μm at 150 W laser power and 1.0 m/s scanning speeds, it increases to 18 μm for 350 W and 2.4 m/s (Figure 19b). Thus, finer particles of Mo after heating by laser beam were melted, while big particles with diameter higher than ~20 μm were partially melted. Ti has higher absorptivity and lower melting point, so it melts first, while Mo particles can heat up but do not reach melting point. Viscosity of liquid Ti at temperatures of 1750-2050 K is 4.42 mPa×s, as has been reported by Paradis *et al.* (2002) and for pure liquid Mo viscosity is 5.39 mPa×s (Iida and Guthrie, 2015). Heavier Mo particles fall down to the bottom of molten pool and transfer quickly their heat to the surrounding alloy. Rather sharp borders between Mo particles and surrounding Ti-Mo alloy was found for big partially melted Mo particles (Figure 20).

At higher laser power, higher temperatures were reached and it was found that there were less unmolten Mo particles in the cross-sections of single layers at 350 W laser power in comparison with 150 W laser power. Rescanning also affected the size of remaining partially melted Mo particles. As a result of rescanning of the bulk material of the first layer, Mo particles reduced in size (Figure 12). At higher scanning speeds, fluid flows were more pronounced and humping effects led to high variability in the track's height (Figure 18) thus creating rougher single layers and high variability in the layer thickness. Thermo-physical conditions for rescanning differ from the first powder layer scanning, also absorptance of solid material is lower than powder material, and thus temperature will be lower in the bulk. The laser energy of rescanning was not enough to fully melt Mo particles trapped into the bottom of the molten pool during first scanning. Therefore, rescanning improved homogeneity of Mo distribution for in the first layer, but not for 3D sample as a whole (Figure 13).

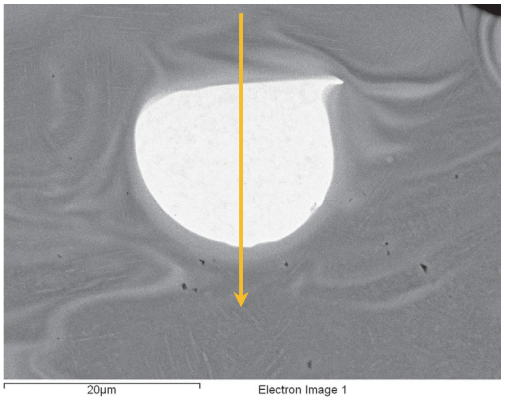

(a)

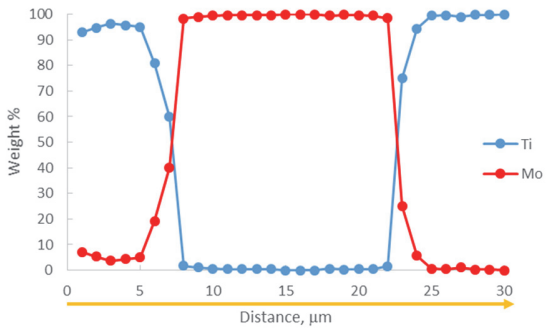

(b)

Figure 20: SEM photo in BSE mode of cross-sections of the first layer manufactured at P=150 W, V=1.0 m/s and 80 µm hatch distance: area with partially melted Mo particle after rescanning (a) and its EDS line spectrum (b).

Complex microstructure with a portion of lamellar structure and areas with cellular dendritic structure was found in *in situ* alloyed 3D LPBF sample (Figure 14). Martis Jr. *et al.* (2011) found similar structure and increased intensity of the peaks of α′-phase of this alloy in Ti15Mo after hot swaging. It was suggested that with fast cooling the structure does not have sufficient time to accommodate a more stable configuration, so the microstructure had irregular grain boundaries (Martins Jr. *et al.*, 2011). Observed average concentrations of Mo in the alloy correspond well to the bi-modal α+β microstructures. Ho *et al.* (1999) indicated that for Ti-*x*Mo alloys when Mo content increased to 10 wt% or higher, retained β phase became the dominant phase.

Analysis of deeply etched specimens revealed that cellular dendritic structures were associated with Mo particles that also confirms higher concentration of Mo in these regions (Figure 15c). Additionally, it was found that the material was inhomogeneous within one track. Due to different concentrations of Mo, different areas resist etching differently and, therefore, specific relief was formed at deep etching. Regions with higher resistance to etching correspond to areas with higher concentration of Mo and follow the solidification front as the melting temperature of Mo is higher. Between the solidification lines, cellular structure with cell size below 1 µm was observed (Figure 15b). These microscopy observations nevertheless have to be confirmed by XRD analysis in the future work.

Ho *et al.* (1999) found that the hardness in alloys with 6–20% of Mo had complex dependence from Mo content and it was suggested that solid solution strengthening, precipitation hardening, strain aging, grain size and phases (α′, α″ and β) could affect the hardness of the Ti–*x*Mo alloy. For the cast Ti15Mo alloy, Martins *et al.* (2014) indicated values of 300–330 HV.

Greater hardness in as-built LPBF Ti15Mo (Figure 16) in comparison with alloy made by conventional method is connected with different thermal history and higher temperature gradients in LPBF process. As-built LPBF Ti6Al4V alloy possessed fine α′ martensitic microstructure had Vickers hardness of 389±14.8 HV (Moletsane *et. al.,* 2016). Ho *et al.* (1999) supposed that as-cast β phase alloys had a higher hardness level than α′ alloys probably due to a

stronger solid solution effect. Ultimate tensile strength (UTS) for as-built LPBF Ti15Mo mini-samples was lower than in LPBF Ti6Al4V samples: 894±23.6 MPa and 1243±49 MPa (Van Zyl *et al., 2016)* correspondingly. Ho (2008) also found that cast Ti15Mo alloy had lower UTS in comparison with Ti6Al4V: 921±19 MPa *versus* 1173±17 MPa.

Conclusions

Determination of optimum process parameters for single tracks and layers for *in situ* LPBF alloying prior to production of 3D objects is to be obligatory. As demonstrated, the combination of the process variables yielded different results which signified non-linear relationships between the various process parameters. *In situ* alloying of blended Ti–Mo powders with similar particle size distributions showed that partially melted Mo particles falled to the bottom of the molten bath. For the selected powders and layer thickness less than 60 μm, transition from conduction to keyhole mode occurred if the ratio of the deposited energy density to the heat of fusion of Ti exceeded 70.

Morphology characterization of the single layers reveals that surface roughness increased with increasing hatch distance; rescanning improved surface quality.

Partially molten Mo particles ~20 μm in diameter were found in single tracks, layers and 3D samples. It can be assumed that using smaller Mo particles would be more preferable. A decreasing particle sizes can deteriorate powder flowability and powder layer deposition. Future research should consider optimal Mo particle sizes to enhance homogeneity of *in situ* alloyed Ti15Mo and its influence on mechanical properties.

In situ alloying was found to be an efficient way to manufacture new materials, nevertheless, to manufacture homogeneous alloy was a challenge. For efficient *in situ* LPBF alloying processes, not only laser power and scanning speed should be optimized. An analysis of materials properties and powder size has to be done in order to guarantee efficient melting and intermixing of both materials. In the present investigations, size of Mo powder was too large and therefore, incomplete melting of Mo powder particles was observed.

Acknowledgements

This work is based on research supported by the South African Research Chairs Initiative of the Department of Science and Technology and the National Research Foundation of South Africa (Grant №97994) and the Collaborative Program in Additive Manufacturing (Contract №CSIR-NLC-CPAM-15-MOA-CUT-01).

References

Aboulkhair, N. T., Maskery, A., Tuck, Ch., Ashcroft, A., Everitt, N. M., 2016. On the formation of AlSi10Mg single tracks and layers in selective laser melting: Microstructure and nano-mechanical properties. *Journal of Materials Processing Technology*, 230, pp. 88-98.

ASTM F2066-13, 2013. ASTM F 2066 S*tandard Specification for Wrought Titanium-15 Molybdenum Alloy for Surgical Implant Applications surgical implant application* (UNSR 8150), West Conshohocken, PA: American Society for Testing Materials.

Chan, C. L., Mazumder, J., Chen, M. M., 1987. Three-dimensional axisymmetric model for convection in laser-melted pools. *Materials Science and Technology*, 3(4), pp. 306-311.

Disegi, J. A., Roach, M. D., McMillan, R. D., Shultzabarger, B. T., 2016. Alpha plus beta annealed and aged Ti-15 Mo alloy for high strength implant applications. *Journal of Biomedical Materials Research Part B: Applied Biomaterials*. 00B:000–000.

Doh, R.M., Pang, N.S., Kim, K.D., Park, W., 2011. Implant displacement into the mandible: an unusual complication during implant surgery. *Implant Dentistry*, 20(5), pp. 345-348.

du Plessis, A., le Roux, S. G., Guelpa, A., 2016. The CT Scanner Facility at Stellenbosch University: An open access X-ray computed tomography laboratory. *Nuclear Instruments and Methods in Physics Research Section B*, 384, pp. 42-49.

Eagar, T. W., Tsai, N. S., 1983. Temperature fields produced by traveling distributed heat sources. *Welding Journal*, 62(12), pp. 346-355.

Fischer, P., Romano, V., Weber, H.P., Karapatis, N.P., Boillat, E., Glardon, R., 2003. Sintering of commercially pure titanium powder with a Nd: YAG laser source. *Acta Materialia*, 51(6), pp. 1651-1662.

Hann, D. B., Iammi, J., Folkes, J., 2011. A simple methodology for predicting laser-weld properties from material and laser parameters. *Journal of Physics D: Applied Physics*, 44(44), p. 445401.

Ho, W. F., 2008. A comparison of tensile properties and corrosion behavior of cast Ti–7.5 Mo with cp Ti, Ti–15Mo and Ti–6Al–4V alloys. *Journal of Alloys and Compounds*, 464(1), pp. 580-583.

Iida, T., Guthrie, R.I.L., 2015. *The thermophysical properties of metallic liquids: Volume 2: Predictive models*, Oxford University Press, 586 p.

Khairallah, S. A., Anderson, A. T., Rubenchik, A., King, W. E., 2016. Laser powder-bed fusion additive manufacturing: Physics of complex melt flow and formation mechanisms of pores, spatter, and denudation zones. *Acta Materialia*, 108, pp. 36-45.

Khairallah, S.A., Anderson, A., 2014. Mesoscopic simulation model of selective laser melting of stainless steel powder. *Journal of Materials Processing Technology*, 214(11), pp. 2627-2636.

King, W.E., Barth, H.D., Castillo, V.M., Gallegos, G.F., Gibbs, J. W., Hahn, D.E., Kamath, C., Rubenchik, A.M., 2014. Observation of keyhole-mode laser melting in laser powder-bed fusion additive manufacturing. *Journal of Materials Processing Technology*, 214(12), pp. 2915-2925.

Kinnear, A., Dzogbewu, T. C., Yadroitsava, I., Yadroitsev, I., 2016. *In situ* alloying process of Ti6Al4V-*x*Cu structures by direct metal laser sintering, in: *Proc. 17th International conference RAPDASA*, 2-4 November 2016, Pretoria, South Africa.

Körner, C., Attar, E., Heinl, P., 2011. Mesoscopic simulation of selective beam melting processes. *Journal of Materials Processing Technology*, 211(6), pp. 978-987.

Körner, C., Bauereiß, A. & Attar, E., 2013. Fundamental consolidation mechanisms during selective beam melting of powders. *Modelling and Simulation in Materials Science and Engineering*, 21(8), p. 085011.

Kou, S., Limmaneevichitr, C. & Wei, P.S., 2011. Oscillatory Marangoni flow: a fundamental study by conduction-mode laser spot welding. *Welding Journal*, 90(12), pp. 229-240.

Król, M., Kujawa, M., Dobrzański, L.A., Tański, T., 2014. Influence of technological parameters on additive manufacturing steel parts in Selective Laser Sintering. *Archives of Materials Science and Engineering*, 67(2), pp. 84-92.

Kruth, J.P., Yasa, E., Deckers, J., 2009. Experimental investigation of laser surface re-melting for the improvement of selective laser melting process. Texas, in: *Proc. of Solid Free Fabrication Symposium*, Austin, Texas, USA, pp. 321-322.

Kruth, J.P., Badrossamay, M., Yasa, E., Deckers, J., Thijs, L., Van Humbeeck, J., 2010. Part and material properties in selective laser melting of metals. s.l., in: *Proc. of the 16th international symposium on electromachining*.

Lee, S.-C., Jeong, C.-H., Im, H.-Y., Kim, S.-Y., Ryu, J.-Y., Yeom, H.-Y., Kim, H.-M., 2013. Displacement of dental implants into the focal osteoporotic bone marrow defect: a report of three cases, *Journal of the Korean Association of Oral and Maxillofacial Surgeons*, 39(2), pp. 94–99.

Leitz, K.H., Singer, P., Plankensteiner, A., Tabernig, B., Kestler, H., Sigl L.S., 2015. Multi-physical simulation of Selective Laser Melting of Molybdenum, in *Proc. of European Congress and Exhibition on Powder Metallurgy. 1-6. Shrewsbury: The European Powder Metallurgy Association.*

Martins, J.R.S., Araújo, Jr.R.O., Donato, T.A.G., Arana-Chavez, V.E., Buzalaf, M.A.R., Grandini, C.R., 2014. Influence of Oxygen content and microstructure on the mechanical properties and biocompatibility of Ti 15 wt%Mo alloy used for biomedical applications. *Materials*, 7, pp. 232–243.

Martins, J.R.S., Jr., Nogueira, R.A., Araújo, R.O.D., Donato, T.A.G., Arana-Chavez, V.E., Claro, A.P.R.A., Moraes, J.C.S., Buzalaf, M.A.R., Grandini, C.R., 2011. Preparation and characterization of Ti–15Mo alloy used as biomaterial. *Materials Research,* 14(1), pp. 107–112.

Matilainen, V.P., Piili, H., Salminen, A., Nyrhilä, O., 2015. Preliminary investigation of keyhole phenomena during single layer fabrication in laser additive manufacturing of stainless steel. *Physics Procedia*, 78, pp. 377-387.

Moletsane, M.G., Krakhmalev, P., Kazantseva, N., du Plessis, A., Yadroitsava, I., Yadroitsev, I., 2016. Tensile properties and microstructure of direct metal laser-sintered Ti6Al4V (ELI) alloy. *The South African Journal of Industrial Engineering*, 27(3), 110-121.

Mumtaz, K., Hopkinson, N., 2010. Selective laser melting of Inconel 625 using pulse shaping. *Rapid Prototyping Journal*, 16(4), pp. 248-257.

Nasab, M.B., Hassan, M.R., Sahari, B.B., 2010. Metallic biomaterials of knee and hip – A review. *Trends in Biomaterials and Artificial Organs*, 24(1), pp. 69-82.

Niinomi, M., Kuroda, D., Fukunaga, K., Morinaga, M., Kato, Y., Yashiro, T., Suzuki, A., 1999. Corrosion wear fracture of new β type biomedical titanium alloys. *Materials Science and Engineering: A*, 263(2), pp. 193-199.

Palik, E. D., 1985. *Handbook of optical constants of solids* (Vol. 1-3). s.l.: Academic press.

Qiu, C, Panwisawas, C., Ward, M., Basoalto, H.C., Brooks, J.W., Attallah, M., 2015. On the role of melt flow into the surface structure and porosity development during selective laser melting. *Acta Materialia*, 96, pp. 72-79.

Rai, R., Elmer, J.W., Palmer, T.A., DebRoy, T., 2007. Heat transfer and fluid flow during keyhole mode laser welding of tantalum, Ti–6Al–4V, 304L stainless steel and vanadium. *Journal of physics D: Applied physics*, 40(18), p. 5753.

Van Zyl, I., Moletsane, M., Krakhmalev, P., Yadroitsava, I., Yadroitsev, I., 2016. Validation of miniaturised tensile testing on DMLS TI6Al4V (ELI) specimens. *The South African Journal of Industrial Engineering*, 27(3), pp. 192-200.

Verhaeghe, F., Craeghs, T., Heulens, J., Pandelaers, L., 2009. A pragmatic model for selective laser melting with evaporation. *Acta Materialia*, 57(20), pp. 6006-6012.

Vrancken, B., Thijs, L., Kruth, J.P., Van Humbeeck, J., 2014. Microstructure and mechanical properties of a novel β titanium metallic composite by selective laser melting. *Acta Materialia*, 68, pp. 150-158.

Wang, D., Yu Ch., Zhou, X., Ma, J., Liu W., Shen, Z., 2017. Dense pure Tungsten fabricated by selective laser melting, *Applied Sciences*, 7(4), pp. 430–443.

Wei, P.S., 2012. The physics of weld bead defects. In: *Welding processes*, ed. R.Kovacevic, InTech DOI: 10.5772/2884, pp. 395-414.

Yadroitsava, I., Els, J., Booysen, G., Yadroitsev, I., 2015. Peculiarities of single track formation from TI6AL4V alloy at different laser power densities by selective laser melting. *South African Journal of Industrial Engineering*, 26(3), pp. 86-95.

Yadroitsev, I., 2009. *Selective laser melting: Direct manufacturing of 3D-objects by selective laser melting of metal powders*. Lambert Academic Publishing, 307 p.

Yadroitsev, I., Bertrand, P. & Smurov, I., 2007. Parametric analysis of the selective laser melting process. *Applied Surface Science*, 253(19), pp. 8064-8069.

Yadroitsev, I., Gusarov, A., Yadroitsava, I., Smurov, I., 2010. Single track formation in selective laser melting of metal powders. *Journal of Materials Processing Technology*, 210(12), pp. 1624-1631.

Yadroitsev, I., Krakhmalev, P., Yadroitsava, I., 2015. Hierarchical design principles of selective laser melting for high quality metallic objects. *Additive Manufacturing*, 7, pp. 45-56.

Yadroitsev, I., Krakhmalev, P. Yadroitsava, I., S. Johansson, Smurov, I., 2013. Energy input effect on morphology and microstructure of selective laser melting single track from metallic powder. *Journal of Materials Processing Technology*, 213(4), pp. 606–613.

Yadroitsev, I., Yadroitsava, I., Bertrand, Ph. Smurov, I., 2012. Factor analysis of selective laser melting process parameters and geometrical characteristics of synthesized single tracks. *Rapid Prototyping Journal*, 18(3), pp. 201-208.

Yang, J., Han, J., Yu, H., Yin, J., Gao, M., Wang, Z., Zeng, X., 2016. Role of molten pool mode on formability, microstructure and mechanical properties of selective laser melted Ti-6Al-4V alloy. *Materials & Design*, 110, pp. 558-570.

Yasa, E., Kruth, J.P., 2008. Experimental study of the combined process of selective laser melting and selective laser erosion, in *Proc. of the RAPID 2008 Conference & Exposition*, Florida, USA, May 20-22.